*lubricants*

MDPI

*Article*

# Numerical Simulations and Experimental Validation of Squeeze Film Dampers for Aircraft Jet Engines

**Markus Golek [1], Jakob Gleichner [1], Ioannis Chatzisavvas [2,*], Lukas Kohlmann [2], Marcus Schmidt [3], Peter Reinke [3] and Adrian Rienäcker [1]**

[1] Institute for Powertrain and Vehicle Technology, University of Kassel, Moenchebergstr. 7, 34125 Kassel, Germany; markus.golek@uni-kassel.de (M.G.); jakob.gleichner@uni-kassel.de (J.G.); adrian.rienaecker@uni-kassel.de (A.R.)
[2] MTU Aero Engines AG, Dachauer Str. 665, 80995 Munich, Germany; lukas.kohlmann@mtu.de
[3] Faculty of Engineering and Health, University of Applied Sciences and Arts Hildesheim/Holzminden/Goettingen, Von-Ossietzky-Straße 99, 37085 Goettingen, Germany; marcus.schmidt@hawk.de (M.S.); peter.reinke@hawk.de (P.R.)
* Correspondence: ioannis.chatzisavvas@mtu.de

**Abstract:** Squeeze film dampers are used to reduce vibration in aircraft jet engines supported by rolling element bearings. The underlying physics of the squeeze film dampers has been studied extensively over the past 50 years. However, the research on the SFDs is still ongoing due to the complexity of modeling of several effects such as fluid inertia and the modeling of the piston rings, which are often used to seal SFDs. In this work, a special experimental setup has been designed to validate the numerical models of SFDs. This experimental setup can be used with various SFD geometries (including piston ring seals) and simulate almost all conditions that may occur in an aircraft jet engine. This work also focuses on the inertia forces of the fluid. The hydrodynamic pressure distribution of a detailed 3D-CFD model is compared with the solution of the Reynolds equation including inertia effects. Finally, the simulation results are compared with experimental data and good agreement is observed.

**Keywords:** squeeze film damper; Reynolds equation; experimental validation; inertia effects; vibrations; rotor dynamics



**Citation:** Golek, M.; Gleichner, J.; Chatzisavvas, I.; Kohlmann, L.; Schmidt, M.; Reinke, P.; Rienäcker, A. Numerical Simulations and Experimental Validation of Squeeze Film Dampers for Aircraft Jet Engines. *Lubricants* **2024**, *12*, 253. https://doi.org/10.3390/lubricants12070253

Received: 29 May 2024
Revised: 27 June 2024
Accepted: 4 July 2024
Published: 13 July 2024



## 1. Introduction

Squeeze film dampers (SFDs) are an essential component in today's aircraft engines, serving to attenuate rotor vibrations excited mainly by mass unbalance or geometric imperfections. High-pressure rotors of modern aircraft engines, for instance, are typically supported with low stiffness in the bearing positions. This places modes with high rotor strain energy well above the operational speed range. In this design concept, the rotor must pass through two rigid body modes at low speeds, which requires damping of the vibration amplitudes at the bearing positions as provided by SFDs. In Figure 1, a typical aircraft jet engine is shown.

The oil–pressure distribution of squeeze film dampers, like standard journal bearing, is calculated using the Reynolds equation [1]. This linear partial differential equation can be approximated with closed-form analytical solutions [2–6]. Due to the limitations of these closed-form solutions, numerical approximations of the full Reynolds equation are usually employed using the Finite Element, the Finite Difference or the Finite Volume methods. Approaches using global ansatz functions such as the global Galerkin approach [7–9] have also been used to find approximate solutions of the Reynolds equation. However, their implementation in complex geometries is more complicated than the local Finite Element approaches.

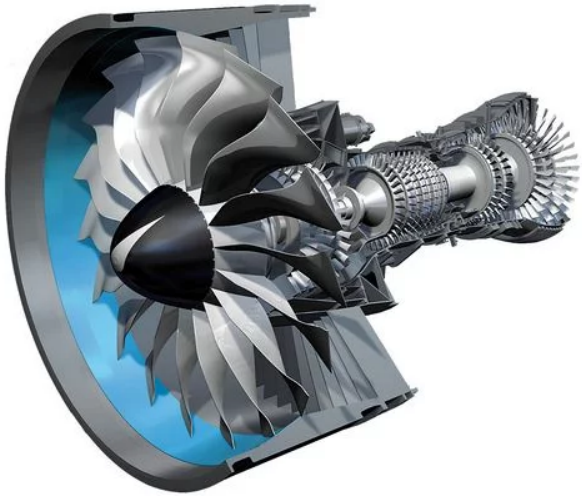

**Figure 1.** Geared turbofan engine PW1100G-JM [10].

Cavitation in hydrodynamic lubrication plays a significant role in the pressure distribution derived from the Reynolds equation. Several approaches have been used in the literature (see, for example, [11]); however, the mass-conserving algorithms such as this described by Kumar and Booker are well established [12].

The thermal effects in the oil are known to influence the pressure distribution in the oil film and thus the hydrodynamic bearing forces. In the work of Dowson [13], the generalized Reynolds equation was developed. A set of integro-differential equations is solved, including the generalized Reynolds and the energy equation of the oil, to obtain the hydrodynamic pressure distribution as well as the 3D temperature field. A detailed discussion on this topic can also be found in [14]. In [15], the thermal effects in the oil including inertia effects have been developed.

The effect of fluid inertia, although typically neglected for journal bearings, may be significant for SFDs. In [16,17], the temporal inertia terms were included in the Reynolds equation. In [18,19], an approach was developed to include both the temporal and the convective inertia terms in the Reynolds equation. This approach increases the computational effort for the calculation of the pressure distribution in the oil, but may significantly improve the physical accuracy of the calculated pressure.

Dedicated experimental results of SFDs are rather scarce in the literature, despite their widespread use. The pioneering work of San Andres focused on the experimental validation of squeeze film damper models (see, for example, [20–22]). The aim of this work is to develop an experimental device similar to the work of [20], which will be able to reproduce all the kinematic conditions (eccentricities, velocities and accelerations) and all the oil-supply conditions (oil-supply pressures and oil-supply temperatures). With minor modifications, this test rig can be used for any SFD geometry, which may include a circumferential groove and/or oil-supply holes or even more complicated geometries. In addition, the influence of the typical sealing mechanisms (piston rings, o-rings, etc.) can be easily quantified. Therefore, this test rig and the results obtained can be used to validate SFD models. In this paper, efficient thermo-hydrodynamic SFD models developed for rotor dynamic simulations and detailed CFD models have been validated.

The main contributions of this work are summarized below:

- A special experimental setup is presented that can be used to validate the SFD bearing forces for all operating conditions that may occur in an aircraft jet engine.
- The SFD bearing forces obtained from the experimental results are compared with those obtained from the numerical simulations and a good agreement is found.
- The 2D solution of the Reynolds equation is compared with a 3D-CFD solution for thin-film lubrication conditions. The influence of inertia effects is shown to be significant for the specific parameter used.

In Section 2, the theory of thermo-hydrodynamic lubrication is presented, including inertia effects and a mass-conserving cavitation algorithm. In Section 3, the experimental setup and its capabilities are discussed. In Section 4, the results are presented, and finally, in Section 5, the main conclusions of this work are summarized.

## 2. Hydrodynamic Lubrication in Squeeze Film Dampers

A typical SFD combined with a rolling element bearing is shown in Figure 2.

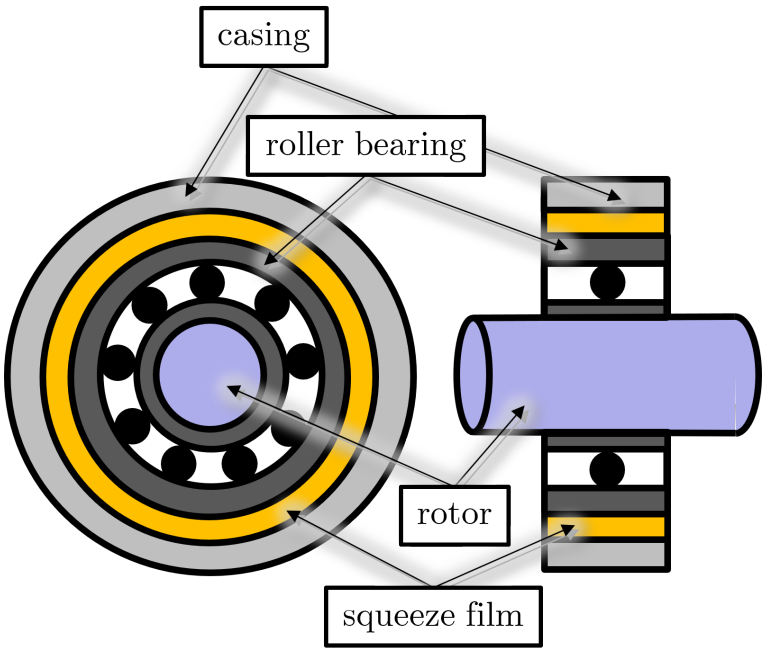


**Figure 2.** Sketch of a rotor supported by a roller bearing with a non-centralized SFD.

In aircraft jet engine applications, SFDs can be centralized or non-centralized (floating rolling element bearing). Centralized SFDs are usually equipped with a squirrel cage (see, for example [23]). The current experimental setup can capture the effects of both SFD designs. In the experimental setup, and therefore in all simulations, oil from a typical oil company for aircraft jet engines was used, namely Mobil Jet Oil II. The dynamic viscosity and density of the oil were used for the hydrodynamics. The oil density, specific heat capacity and thermal conductivity were used in the thermal model.

### *2.1. Thermo-Hydrodynamic Modeling*

The thermo-hydrodynamic modeling described in this work is based on the generalized Reynolds equation and the Energy equation developed in [13] combined with a mass-conserving cavitation algorithm from [12], including the inertia effects from [18].

#### 2.1.1. Generalized Reynolds Equation with a Mass-Conserving Cavitation Algorithm

The generalized Reynolds equation is solved using the Finite Element Method on a 2D mesh. As the oil cannot withstand high negative pressures, a cavitation model is used in combination with the Reynolds equation. The simplest approach is to use the Gümbel cavitation approach, which simply sets all negative pressures to zero [14,24], violating the conservation of mass. To ensure mass conservation, Kumar and Booker [12] provide an algorithm for tracking the density $\bar{\rho}$ of a mixture of oil and gas in the spatial/temporal diverging gap. The viscosity of the mixture is assumed to behave in the same way: $\bar{\rho}/\bar{\rho}_{oil} = \bar{\eta}/\bar{\eta}_{oil}$. This prevents non-physical oil flow in the cavitation region as observed with non mass-conserving procedures. The algorithm divides the fluid film into different regions that must be identified:

- Region 1a ($\bar{\rho} = \bar{\rho}_{oil}, \partial\bar{\rho}/\partial t = 0$);

- Region 1b ($\bar{\rho} = \bar{\rho}_{oil}, \partial\bar{\rho}/\partial t < 0$);
- Region 2 ($\bar{\rho} < \bar{\rho}_{oil}$).

The transition between the full-film regions 1a and 1b is a complementary problem that is solved iteratively. After using an Euler-explicit time integration scheme, nodes are moved between regions 1a and 2. Equation (1) shows the generalized Reynolds equation used to calculate the hydrodynamic pressure in the oil:

$$\frac{\partial}{\partial x}\left(\bar{\rho}F_1\frac{\partial p_0}{\partial x}\right) + \frac{\partial}{\partial y}\left(\bar{\rho}F_1\frac{\partial p_0}{\partial y}\right) = \frac{\partial}{\partial x}(\bar{\rho}u_J F_2) + h\frac{\partial\bar{\rho}}{\partial t} + \bar{\rho}\frac{\partial h}{\partial t}, \tag{1}$$

where $h$ is the gap function and $p_0$ is the pressure distribution. The $x$-coordinate represents the circumferential direction and the $y$-coordinate represents the axial direction of the SFD. The Reynolds equation balances the fluid flows caused by pressure gradients on the left-hand side of the equation and by shearing, density changes and squeezing on the right-hand side. Figure 3a shows the pressure distribution in the oil of an SFD, where the cavitation area is determined by the Kumar–Booker algorithm. Figure 3b compares the pressure distribution over the circumferential coordinate at the axial centerline $b = 0$. The Kumar–Booker algorithm provides the spatial and temporal evolution of the the cavitation area. The size of the cavitation area can have a large effect on the pressure distribution and therefore on the hydrodynamic bearing forces. Due to mass conservation, the Kumar–Booker model is required to determine the oil flow out of the SFD. Therefore, all experimental results are compared with the simulation results using the Kumar–Booker cavitation model.

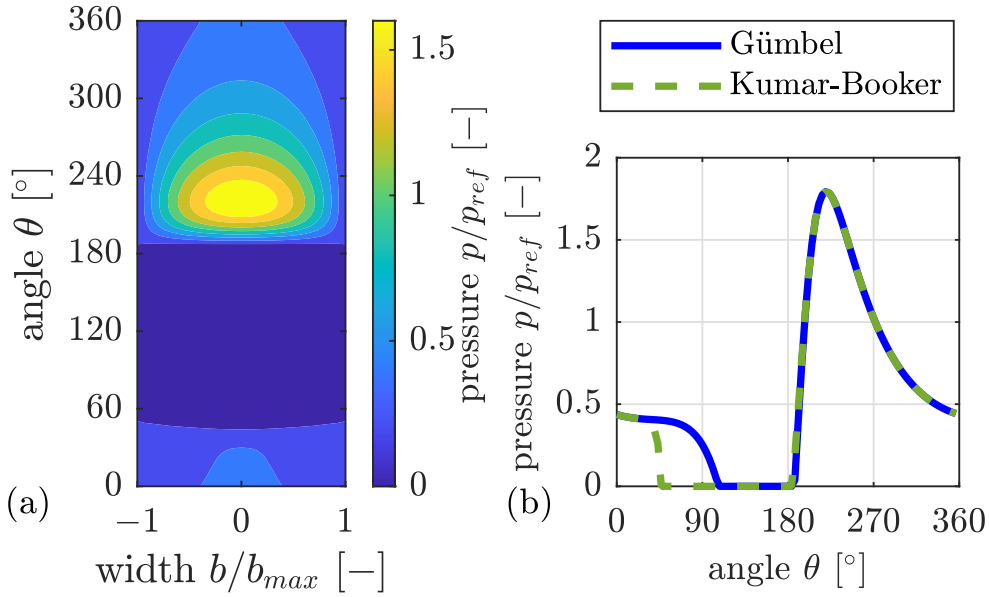


**Figure 3.** (**a**) Oil–pressure distribution in the SFD with Kumar–Booker cavitation model. (**b**) Comparison of oil–pressure with different cavitation models.

Figure 4 shows the evolution of the density in the SFD over the circumferential coordinate at the axial centerline $b = 0$. At the beginning of the orbit at time $t_0$, the gap is completely filled with oil. In this case, the density and the cavitation area evolve within a third of an orbit ($t_1$ to $t_4$) and from then on follow the high-pressure field, only changing their position according to the orbit (compare $t_4$ and $t_5$).

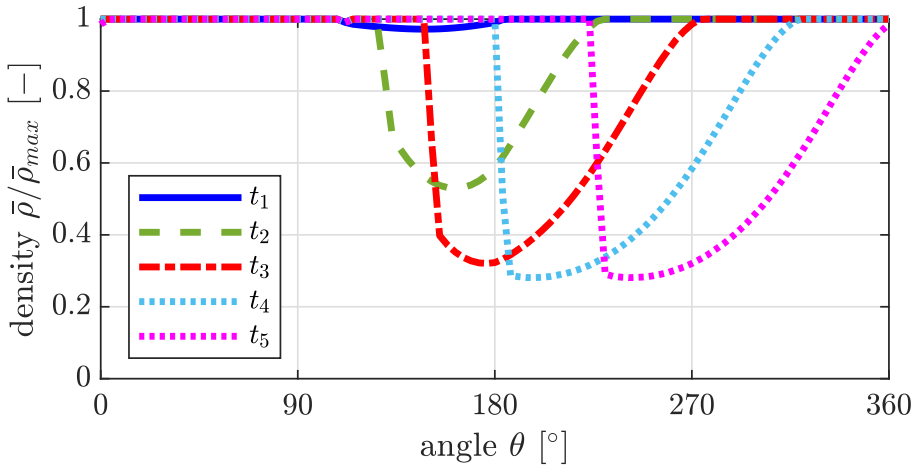


**Figure 4.** Density evolution with Kumar–Booker cavitation model.

The temperature distribution in the oil film is not constant. Isothermal models may offer simplicity in the implementation and in the solution procedure but they neglect the variable temperature field in the oil film and cannot account for effects such as temperature differences of the oil inlet, journal and casing. To account for these effects, integrals of viscosity across over the gap height are introduced at each node of the 2D mesh [13], as shown in Equation (2):

$$F_1 = J_{2h} - \frac{J_{1h}^2}{J_{0h}}, \quad F_2 = \frac{J_{1h}}{J_{0h}}, \quad J_{0h} = \int_0^h \frac{1}{\eta} dz, \quad J_{1h} = \int_0^h \frac{z}{\eta} dz, \quad J_{2h} = \int_0^h \frac{z^2}{\eta} dz. \tag{2}$$

Isothermal modeling with constant viscosity over gap height leads to the more commonly known equation derived in [13,25] with $F_1 = h^3/12\eta$ and $F_2 = h/2$. Here, the oil viscosity is not constant across the gap height ($z$-direction). $J_{0h}$, $J_{1h}$ and $J_{2h}$ are necessary to integrate viscosity considering various exponents of the gap height $h$. By introducing a parabolic 'global' ansatz function for the temperature across the gap, the need to include a 3D mesh for the energy equation is avoided, heavily reducing the computational cost. In order to determine the temperature distribution along and across the oil film, the energy equation for fluids has to be solved simultaneously.

### 2.1.2. Temporal and Convective Inertia in the Reynolds Equation

Hamzehlouia in [18] developed a model that can approximate the pressure distribution in fluid film bearings including inertia effects. Based on a perturbation calculation and assuming that inertia has no effect on the fluid velocities, Hamzehlouia derived an extended Reynolds Equation (3) from the Navier–Stokes equations that includes inertia terms.

$$\frac{\partial}{\partial x}\left(\bar{\rho}F_1\frac{\partial p_1}{\partial x}\right) + \frac{\partial}{\partial y}\left(\bar{\rho}F_1\frac{\partial p_1}{\partial y}\right) = \frac{\partial}{\partial x}\left(\bar{\rho}u_J F_2\right) + h\frac{\partial \bar{\rho}}{\partial t} + \bar{\rho}\frac{\partial h}{\partial t} + G_1(x,y) + G_2(x,y). \tag{3}$$

where $G_1$ and $G_2$ are the extended parts and depend on the pressure distribution without inertia effects. $G_1$ in Equation (4) describes the temporal (fluid flow caused by change in fluid velocity over time) inertia and $G_2$ in Equation (5) takes convective (fluid flow caused by a change in the fluid velocity due to its change in position) inertia into account:

$$G_1(x,y) = \frac{\bar{\rho}^2}{12\bar{\eta}}\left(h^2\frac{\partial^2 h}{\partial t^2} + \frac{h}{6\bar{\eta}}\frac{\partial h}{\partial x}\left(h^3\frac{\partial^2 p_0}{\partial t \partial x} + 3h^2\frac{\partial h}{\partial t}\frac{\partial p_0}{\partial x}\right)\right). \tag{4}$$

$$
\begin{aligned}
G_2(x,y) = \frac{\bar{\rho}^2}{12\bar{\eta}^3}\Bigg( & -\frac{5h^5}{20}\left(\frac{\partial h}{\partial x}\right)^2\left(\frac{\partial p_0}{\partial x}\right)^2 - \frac{5h^6}{144}\frac{\partial^2 h}{\partial x^2}\left(\frac{\partial p_0}{\partial x}\right)^2 - \frac{5h^6}{72}\frac{\partial h}{\partial x}\frac{\partial p_0}{\partial x}\frac{\partial^2 p_0}{\partial x^2} \\
& - \frac{7h^6}{72}\frac{\partial h}{\partial x}\frac{\partial p_0}{\partial x}\frac{\partial^2 p_0}{\partial x^2} - \frac{h^7}{72}\left(\frac{\partial^2 p_0}{\partial x^2}\right)^2 - \frac{h^7}{72}\frac{\partial p_0}{\partial x}\frac{\partial^3 p_0}{\partial x^3} \\
& - \frac{7h^6}{144}\frac{\partial h}{\partial x}\frac{\partial^2 p_0}{\partial x \partial y}\frac{\partial p_0}{\partial y} - \frac{h^7}{144}\frac{\partial^3 p_0}{\partial x^2 \partial y}\frac{\partial p_0}{\partial y} - \frac{h^7}{144}\left(\frac{\partial^2 p_0}{\partial x \partial y}\right)^2 \\
& - \frac{7h^6}{144}\frac{\partial h}{\partial x}\frac{\partial p_0}{\partial x}\frac{\partial^2 p_0}{\partial y^2} - \frac{h^7}{144}\frac{\partial^2 p_0}{\partial x^2}\frac{\partial^2 p_0}{\partial y^2} - \frac{h^7}{144}\frac{\partial p_0}{\partial x}\frac{\partial^3 p_0}{\partial x \partial y^2} \\
& - \frac{5h^6}{144}\frac{\partial h}{\partial x}\frac{\partial^2 p_0}{\partial x \partial y}\frac{\partial p_0}{\partial y} - \frac{5h^6}{144}\frac{\partial h}{\partial x}\frac{\partial p_0}{\partial x}\frac{\partial^2 p_0}{\partial y^2} - \frac{h^7}{144}\frac{\partial^3 p_0}{\partial x \partial y^2}\frac{\partial p_0}{\partial x} \\
& - \frac{h^7}{144}\left(\frac{\partial^2 p_0}{\partial x \partial y}\right)^2 - \frac{h^7}{144}\frac{\partial^2 p_0}{\partial y^2}\frac{\partial^2 p_0}{\partial x^2} - \frac{h^7}{144}\frac{\partial p_0}{\partial y}\frac{\partial^3 p_0}{\partial x^2 \partial y} - \frac{h^7}{72}\left(\frac{\partial^2 p_0}{\partial y^2}\right)^2 \\
& - \frac{h^7}{72}\frac{\partial p_0}{\partial y}\frac{\partial^3 p_0}{\partial y^3}\Bigg).
\end{aligned} \tag{5}
$$

The extension term $G_1$ consists primarily of the gap function and the time derivatives of the gap function. $G_2$ depends mainly on the pressure gradients, the gap function and the gradient of the gap function in circumferential direction. The gap is assumed to be constant in axial direction [18]. Solving Equation (1) gives the pressure distribution $p_0$ without inertia effects. It is used in Equation (3) to return the pressure distribution $p_1$, including the complete inertia. San Andrés provides the implementation of temporal inertia effects with linearization without a perturbation method and by neglecting the pressure gradients, as shown in Equation (6) [26]:

$$
G_1(x,y) = \frac{\bar{\rho}^2 h^2}{12\bar{\eta}}\frac{\partial^2 h}{\partial t^2}; \quad G_2(x,y) = 0. \tag{6}
$$

This model is more time efficient, and compared to Hamzehloiuia's temporal inertia effects, the results are very similar. Figure 5 shows the forces $F_x$ and $F_y$ for a circular orbit around the centerline.

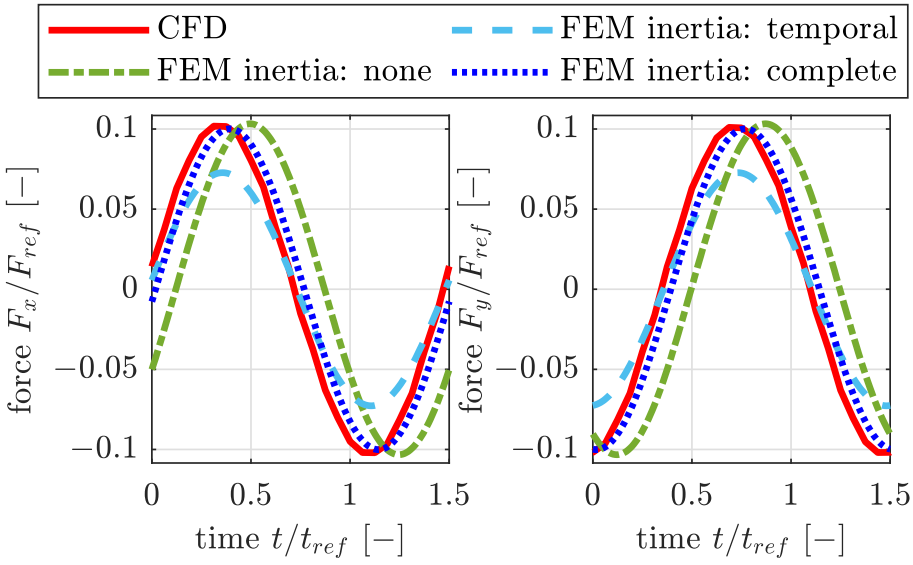


**Figure 5.** Comparison of inertia models for circular orbits around centerline.

A 3D-CFD simulation is assumed to provide the reference solution for the hydrodynamic bearing forces. The 3D-CFD simulations of the two-phase fluid flow inside the SFD were performed using the code OpenFOAM, which is based on the finite volume method

and uses time-dependent, three-dimensional, incompressible Navier–Stokes equations. The computational domain of the simulation is enclosed by three geometrical boundaries: the inner moving solid wall, the outer fixed solid wall and the axial open ends of the fluid film. In the numerical setup, individual boundary conditions must be specified for the flow variables. Zero gradient conditions apply for pressure and volume fraction at the fixed solid walls, as well as no-slip conditions for the velocity. At the open ends, the ambient pressure is specified and the volume fraction is set to one. The dynamic mesh motion is defined by the displacement of the boundary points. For this purpose, the temporal and spatial displacement of the inner moving wall is implemented and a velocity distribution of each individual mesh point is obtained. The moving mesh is characterized by stretching and squeezing of the volume cells within the fluid film, which results in a change in the local film thickness. In the previous work of Schmidt et al. [27] and Reinke et al. [28], it was determined that a minimum number of cells must be applied to the squeeze film in the radial direction. The sensitivity test of a squeezed lubrication film carried out showed that six cells applied across the film achieves the acceptable radial resolution for the expected flow conditions. The overall mesh size contains 2.8 million cells with respect to the cell aspect value due to cell deformation, which is below the maximum value of 10 proposed by Kistner [29].

FEM solutions without any inertia effects, with temporal inertia effects only and with complete (temporal + convective) inertia effects are generated. The FEM solution without inertia effects has almost the same amplitude as the FEM solution with complete inertia, but there is a phase shift between these two solutions. The complete inertia model shows a better agreement with the 3D-CFD results. The temporal inertia model shows the largest deviation from the 3D-CFD results in this case. In Figure 6, the same comparison is performed as in Figure 5 but with an off-centered orbit.

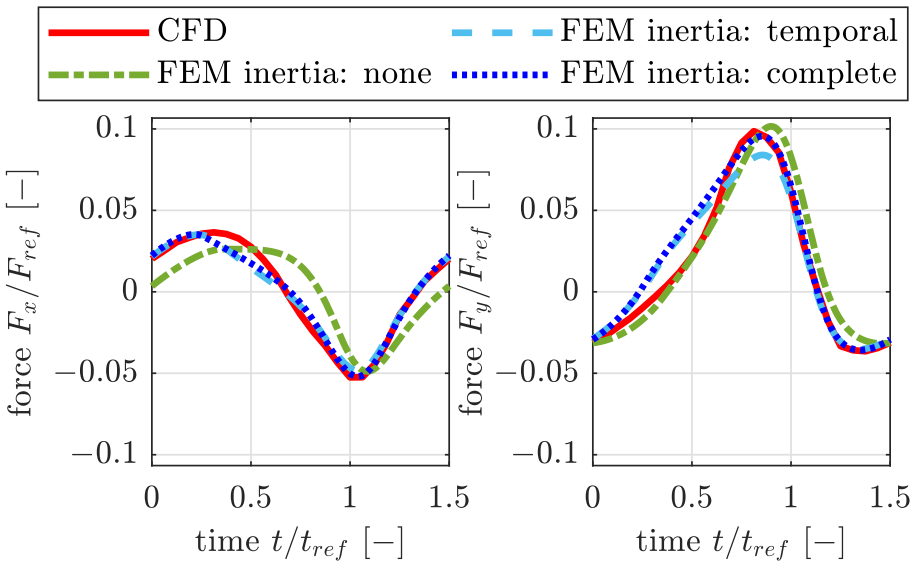


**Figure 6.** Comparison of inertia models for circular orbits around off-center position.

The complete inertia model once again shows a better agreement with the reference 3D-CFD solution.

2.1.3. Energy Equation in the Oil Film

The energy equation of the oil shown in Equation (7) is simplified by considering similar order-of-magnitude assumptions as in the Reynolds equation [30]:

$$h\bar{\rho}\bar{c}_p\left(\bar{u}\frac{\partial\overline{T}}{\partial x}+\bar{v}\frac{\partial\overline{T}}{\partial y}\right)-\frac{\partial}{\partial x}\left(h\bar{\lambda}\frac{\partial\overline{T}}{\partial x}\right)-\frac{\partial}{\partial y}\left(h\bar{\lambda}\frac{\partial\overline{T}}{\partial y}\right)-\bar{\lambda}\left[\frac{\partial T}{\partial z}\right]_0^h=\bar{\phi}_{hyd}. \tag{7}$$

On the left-hand side are the convection and conduction terms, and on the right-hand side is the hydrodynamic dissipation as a source of energy. The equation is integrated over the gap height to solve it on the same 2D mesh as the pressure distribution. The fluid velocities (Equation (8)) and the hydrodynamic dissipation (Equation (9)) are integrated over the gap height using the Dowson integrals from Equation (2):

$$\begin{aligned} \bar{u} &= -\frac{F_1}{h}\frac{\partial p_1}{\partial x} + \frac{u_J}{h}F_2, \\ \bar{v} &= -\frac{F_1}{h}\frac{\partial p_1}{\partial y}, \end{aligned} \tag{8}$$

$$\bar{\phi}_{hyd} = \frac{u_J^2}{J_{0h}} + F_1\left(\frac{\partial p_1}{\partial x}\right)^2 + F_1\left(\frac{\partial p_1}{\partial y}\right)^2. \tag{9}$$

To calculate these terms, the pressure distribution $p_1$ and the velocity of the journal $u_J$ are required [31].

### 2.2. Finite Element Formulation of the Thermo-Hydrodynamic Equations

The Reynolds equation is solved using the Finite Element Method on a 2D mesh. The FE formulation is given in Equation (10) [25,31]:

$$\begin{aligned} &\int_\Omega \bar{\rho}F_1\left(\frac{\partial \psi_i}{\partial x}\frac{\partial \psi_j}{\partial x} + \frac{\partial \psi_i}{\partial y}\frac{\partial \psi_j}{\partial y}\right)d\Omega \cdot p_{1j} = \\ &\int_\Omega \left(\bar{\rho}_u u_J F_2 \frac{\partial \psi_i}{\partial x} + \frac{\partial \bar{\rho}}{\partial t}h\psi_i + \bar{\rho}\frac{\partial h}{\partial t}\psi_i + G_1(x,y)\psi_i + G_2(x,y)\psi_i + \dot{m}_\Omega \psi_i\right)d\Omega + \int_\Gamma \dot{m}_\Gamma \psi_i d\Gamma. \end{aligned} \tag{10}$$

The Reynolds equation is now a hyperbolic differential equation with a space-and-time-dependent density. If the problem has dominant convection, the numerical solution will show non-physical oscillations. Therefore, upwinding techniques are necessary to remove these oscillations [32]. Following this path, $\bar{\rho}_u$ is the upwind density. To integrate the density $\bar{\rho}_u$, a term is added to the shape function $\psi_i$ to move the integration point streamline upwards. The added term mostly depends on the stream direction $u_J/|u_J|$. This is called the streamline upwind Petrov–Galerkin (SUPG) method [33]. Using this method, oscillations in the axial direction may still occur if the density gradient in the axial direction is high due to pressure/density boundaries at the SFD ends and lower cavitation pressure. Discontinuity Capturing solves this problem by adding another term to $\psi_i$, which is controlled by the sign of the density gradient in axial direction $(\partial\bar{\rho}/\partial y)/|\partial\bar{\rho}/\partial y|$ [34]. Equation (11) shows the FE formulation of the energy equation for fluids.

$$\begin{aligned} &\int_\Omega \left\{ W_i\left(h\bar{\rho}\bar{c}_p\left(\bar{u}\frac{\partial \psi_j}{\partial x} + \bar{v}\frac{\partial \psi_j}{\partial y}\right) + \frac{\bar{\lambda}}{h}12\psi_j\right) + h\bar{\lambda}\left(\frac{\partial \psi_i}{\partial x}\frac{\partial \psi_j}{\partial x} + \frac{\partial \psi_i}{\partial y}\frac{\partial \psi_j}{\partial y}\right)\right\}d\Omega \cdot \overline{T}_j = \\ &\int_\Omega \left\{ W_i\left(\bar{\phi}_{hyd} + 6\frac{\bar{\lambda}}{h}(T_J + T_C)\right)\right\}d\Omega. \end{aligned} \tag{11}$$

It is solved on the same 2D mesh as the hydrodynamic pressure equation. This diffusion-convection problem is also typically convection-dominated, making upwinding necessary to obtain useful results [31]. SUPG is also used here to remove oscillations. The shape function $\psi_i$ is extended by a perturbation term $P_i$ to move the integration points streamline upwards like $W_i = \psi_i + P_i$. Stream direction can be identified by the fluid velocities $\bar{u}$ and $\bar{v}$ to account for circumferential and axial flow. Unlike the density in the Reynolds equation, all shape functions of the energy equation are modified by the upwinding term [31,32].

## 3. Experimental Setup

Despite the significant efforts to understand and mathematically describe the mechanics of squeeze film damping, the SFD system is complicated and—in the presence of piston ring sealing and deep circumferential grooves—exhibits areas which are not yet well understood and analyzed. An experimental validation is therefore imperative to demonstrate the benefits and shortcomings of the analytical techniques employed. In Figure 7, a novel test rig, operated at the University of Kassel (UKS), is shown in order to perform full-scale tests of squeeze film dampers (SFD). It consists of a shaft that is enabled by the design of the suspension to perform an orbital motion.

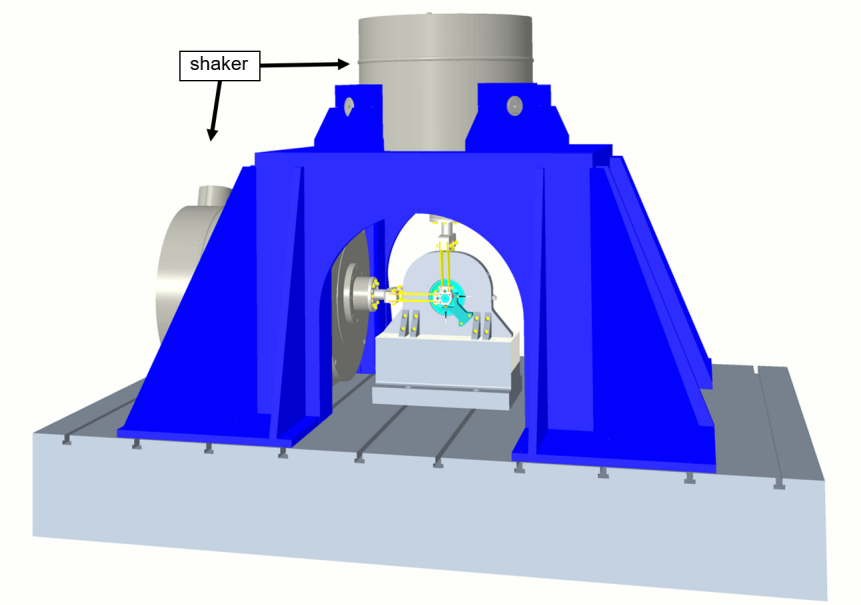


**Figure 7.** CAD view.

Two electromagnetic shakers, one for vertical and one horizontal direction, cause the shaft to move on a pre-described orbit. During operation, shaft and housing are separated by a thin pressurized oil film, which simulates restoring forces comparable to an unbalanced loading of a rotating shaft. Due to its modular design, the test rig can be operated with different bearing geometries regarding clearance, groove or oil-supply holes. Similar to the test rig of San Andrés, the circular motion is realized by control of the input of the two shakers [20–22].

In comparison to the test rig of San Andrés, the shaft of the UKS test rig executes the circular movement and is directly mounted to the shakers without additional support. The shaft has similar dimensions to San Andrés, and under operation, the relative eccentricities can reach up to 0.9. Additionally, the dimensions of the test rig has been optimized to shift the natural frequencies of the moving parts above the operating range. In this way, tests at high operating frequencies can be performed, which cover the typical range of rotational speeds of aero engines.

The main mechanical components of the system under test are shaft, housing, force measuring flanges and spring sheets connecting the shaft to the shakers (Figure 8). The orbital motion of the shaft is enabled by use of spring sheets with a high axial stiffness to transmit the forces provided by the shakers. Laterally, the plates are flexible to minimize the reaction forces on the perpendicular axes. The scaling of the smaller shaft, in contrast to the larger shaft, allows the test stand to reach all operating points. In the case of the the larger shaft, occurring accelerations and forces render reaching operating points impossible. The oil is pre-heated within a heat exchanger and supplied to the pressurized film by an oil pump. Prior to test runs, the test rig is heated by the oil flow for several hours until constant temperature of shaft and housing is reached. In addition to temperature, different

inlet oil pressures, operating frequencies and eccentricities can be set. Additionally, the SFD test rig can be supplemented with piston rings and a circumferential oil-supply groove in the housing. Figure 9 shows the test rig setup at the University of Kassel.

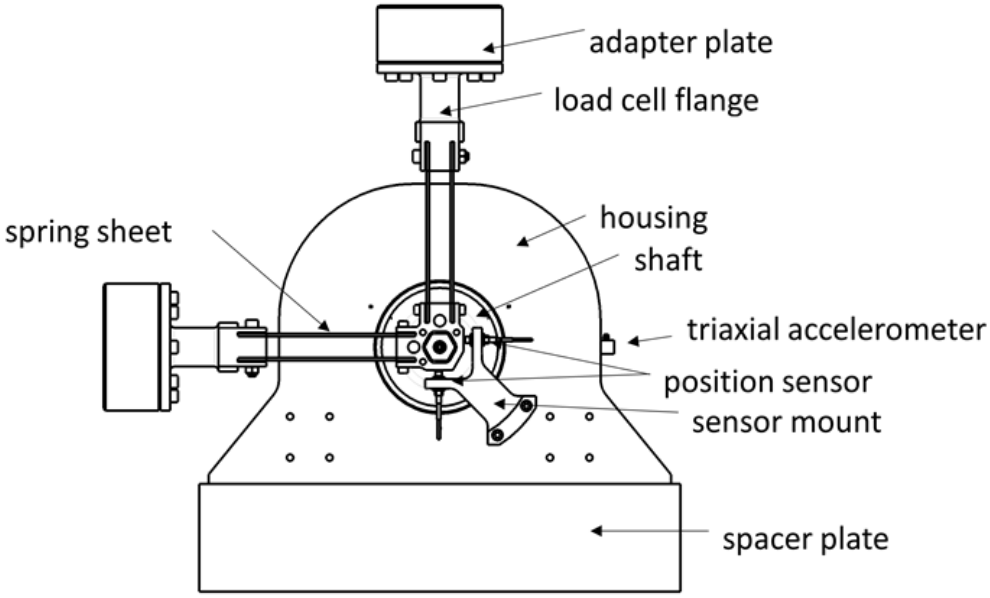


**Figure 8.** Schematic view.

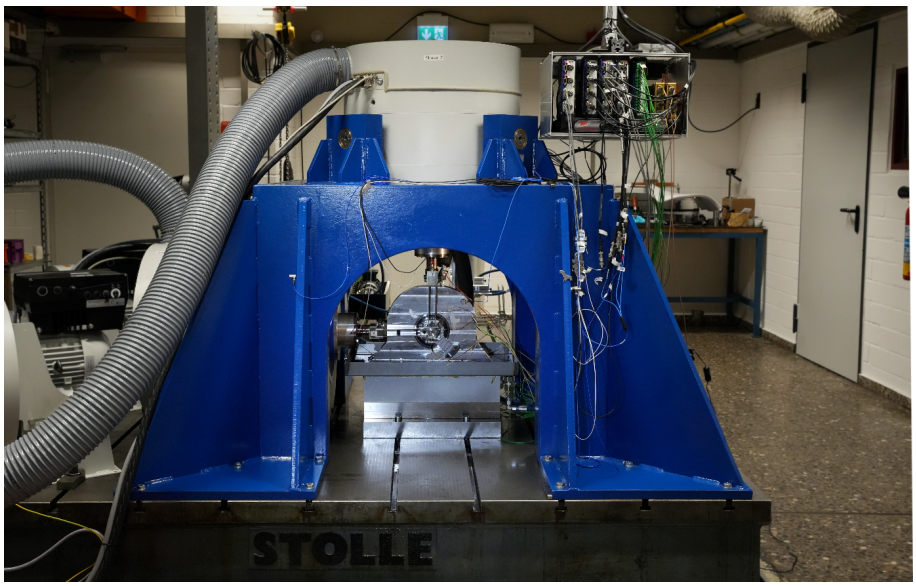


**Figure 9.** Squeeze film damper test rig at the University of Kassel.

The central parameters on this test stand are measured and recorded at various points. This includes 17 temperature measuring points located inside and outside of the shaft housing, the shaft and oil supply. Additionally, sensors for volume flow and oil pressure (3×) are mounted within the oil system. Measurement setup is completed by five accelerometers located on housing, each shaker table and frame. The most important measurement variables include force and displacement. Figure 10 shows a detailed view of the test rig, highlighting the position of the measured variables.

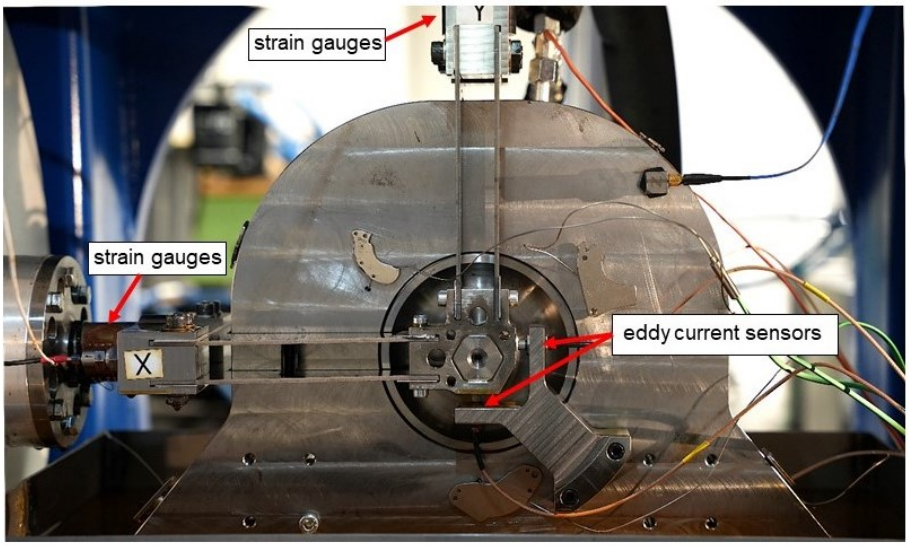


**Figure 10.** Detailed view of the housing with shaft.

Both shakers are connected to the spring plates by a force measuring flange. These flanges are equipped with strain gauges and have been force-calibrated prior to the measurement campaign in a universal testing machine. The orbit of the shaft is measured on both sides of the housing by two eddy current sensors and used to control the shakers. For each test, an inlet oil pressure and temperature is set and both stationary and transient operating points of frequency and eccentricity can be conducted by the dynamic control scheme. In addition, a second control loop can be applied to move the center line of the shaft statically in the housing and maintaining the desired position throughout the test. Positioning of the shaft is a crucial step carried out after every modification to the experimental setup. The position of the shaft in the housing is of central importance for the results of the test. Even small changes will result in a large effect on the resulting forces and the position of the orbits. However, it is not possible to determine the absolute position of the shaft in relation to the housing as the eddy current sensors can only measure the relative position of the shaft. The absolute position of the shaft relative to the housing is determined by the alignment curve. The alignment curve, which is also important for determining the static and dynamic eccentricity of each test point, is traced through the static movement of the shaft in the housing over the full circumference under a defined force.

In order to compare hydrodynamic forces of the test rig results with simulation, the inertia forces of the moving components have to be subtracted from the measured forces. The forces caused by bending of the spring sheets are very small compared to the fluid forces and can be neglected.

## 4. Results and Discussion

The comparison of measurement and simulation covers the range of one orbit around a slightly off-centered position (see Figure 11). The amplitudes of the measured eccentricities in both directions, $x$ and $y$, are almost equal, which means the orbit is more circular than elliptical. The phase shift between $e_x$ and $e_y$ is 90°.

Figure 12 shows the meshed SFD model which is used to solve the Reynolds and energy equation. The experimental setup used a typical aircraft engine SFD length ($L$)-to-diameter ($D$) ratio of $L/D = 0.2$. At the side ends of the SFD, pressure is set to atmospheric pressure. Oil flows into the SFD through three feed holes where the measured flow is set as the natural boundary condition. The algorithm of Kumar and Booker exhibits a large cavitation area (marked with dark blue). At inlet holes, the cavitation area decreases over time as the oil flows in.

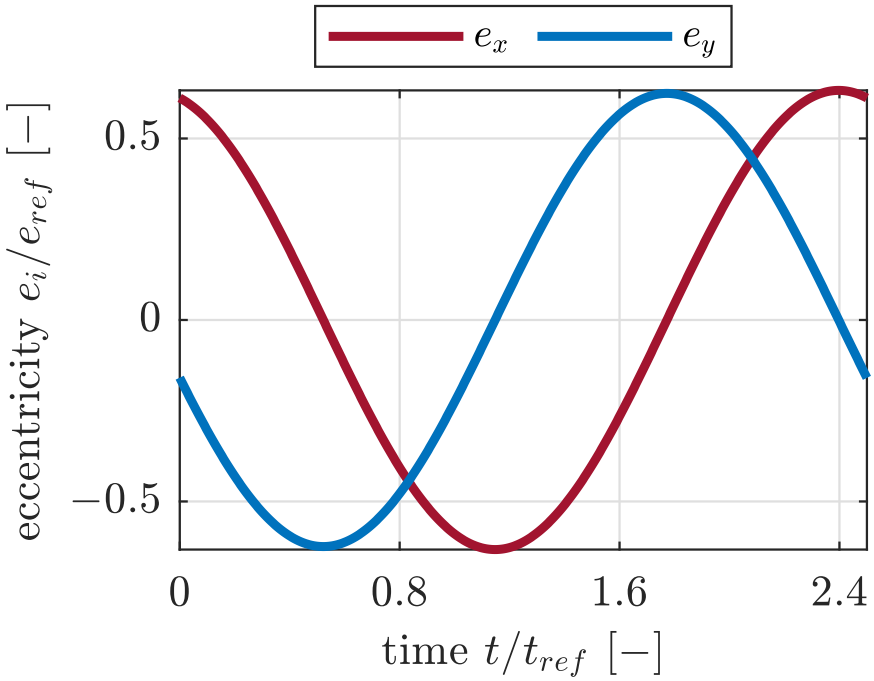


**Figure 11.** Eccentricity of measurement.

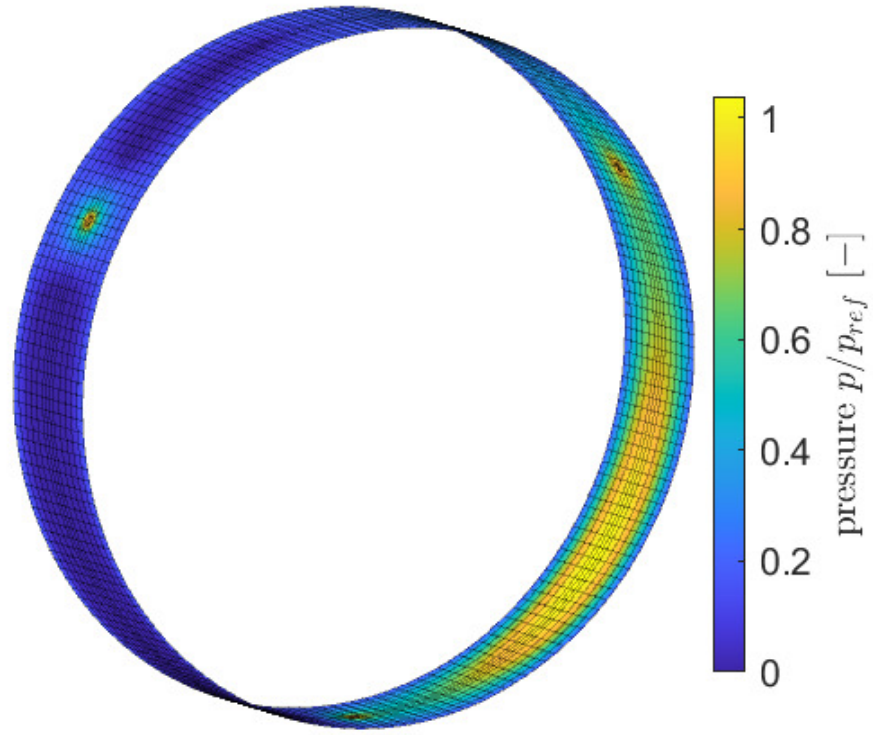


**Figure 12.** SFD mesh with exemplary pressure distribution.

For the given motion as given in Figure 11, both the resulting forces within the experiment and the calculated forces from the simulation can be compared. Figure 13 shows a good correlation of measurement and simulation for $F_x$ and $F_y$. Except for the deviation around $t/t_{ref} = 1$, amplitude matches well and the phase is almost identical.

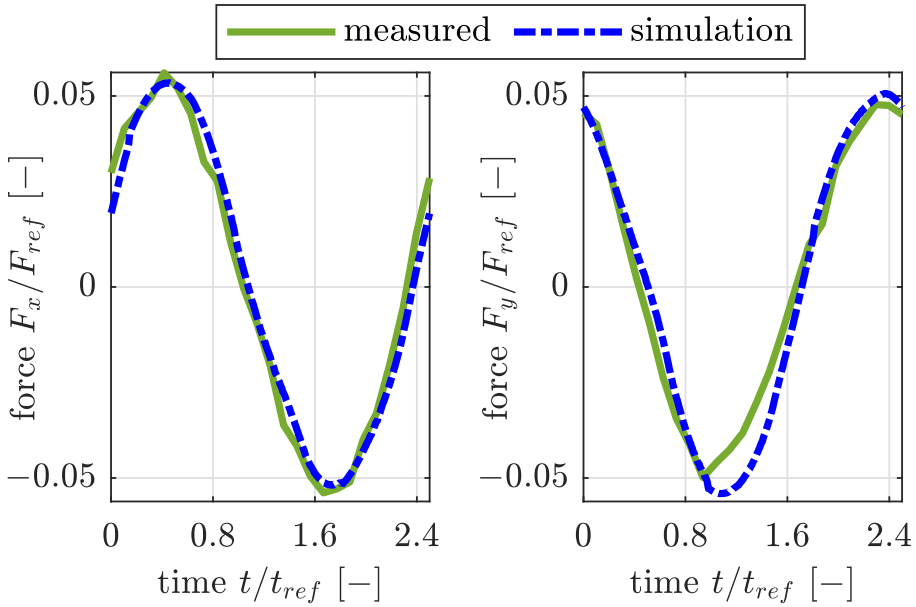


**Figure 13.** Forces $F_x$ and $F_y$ of measurement.

Oil flow out of the SFD's ends is shown in Table 1. It is averaged over one orbit. The deviation of measurement and simulation is shown below.

**Table 1.** Comparison of oil flow out of the SFD.

| Measured $q/q_{ref}$ [−] | Simulation $q/q_{ref}$ [−] | Rel. Deviation |
|---|---|---|
| 0.450 | 0.422 | 6.22% |

## 5. Conclusions

In this work, an experimental setup for the validation of models of squeeze film dampers has been presented. Detailed thermo-hydrodynamic SFD bearing models were developed by focusing on inertia, cavitation and thermal effects. The 2D FEM models based on the Reynolds equation were compared with 3D-CFD models. It was shown that the inertia effects should be taken into account when high physical accuracy is required. Furthermore, the numerical simulation results were compared with experimental data and showed a very good agreement. This work is currently being extended to squeeze film dampers with a circumferential groove and piston rings. Different oil-supply pressures, oil-supply temperatures, different bearing eccentricities and different orbiting speeds are considered. In order to compare between different SFDs, the inertia and damping coefficients will be extracted from the experimental data. A comparison will also be made with the coefficients obtained from the numerical simulations. Finally, back-to-back experiments will be performed with and without oil in the SFD to identify the influence of the SFD forces.

**Author Contributions:** Conceptualization, I.C. and A.R.; methodology, M.G., I.C. and A.R.; software, M.G., M.S. and A.R.; validation, J.G., M.G., L.K. and A.R.; writing—original draft preparation, M.G., J.G. and I.C.; writing—review and editing, I.C., L.K., M.S. and A.R.; visualization, M.G. and J.G.; supervision, I.C., L.K., A.R. and P.R.; project administration, I.C. All authors have read and agreed to the published version of the manuscript.

**Funding:** This research was partially funded by WTD 61/Bundeswehr.

**Data Availability Statement:** Data are not made available due to confidentiality reasons.

**Acknowledgments:** The authors would like to thank MTU Aero Engines for the permission to publish this work.

**Conflicts of Interest:** Authors Ioannis Chatzisavvas and Lukas Kohlmann were employed by the company MTU Aero Engines AG. The remaining authors declare that the research was conducted in the absence of any commercial or financial relationships that could be construed as a potential conflict of interest.

## References


1. Reynolds, O. IV. On the theory of lubrication and its application to Mr. Beauchamp tower's experiments, including an experimental determination of the viscosity of olive oil. *Philos. Trans. R. Soc. Lond.* **1886**, *177*, 157–234.
2. Dubois, G.B.; Ocvirk, F.W. The short bearing approximation for plain journal bearings. *Trans. Am. Soc. Mech. Eng.* **1955**, *77*, 1173–1178. [CrossRef]
3. Yamamoto, T.; Ishida, Y. *Rotordynamics: A Modern Treatment with Applications*; Wiley: Hoboken, NJ, USA, 2001.
4. Della Pietra, L.; Adiletta, G. The Squeeze Film Dampers over Four Decades of Investigations. Part I: Characteristics and Operating Features. *Shock Vib. Dig.* **2002**, *34*, 3–26.
5. Hori, Y. *Hydrodynamic Lubrication*, 1st ed.; Springer: Tokyo, Japan, 2006. [CrossRef]
6. Szeri, A.Z. *Fluid Film Lubrication*; Cambridge University Press: Cambridge, UK, 2010.
7. Someya, T. Stabilität einer in zylindrischen Gleitlagern laufenden, unwuchtfreien Welle: Beitrag zur Theorie des instationär belasteten Gleitlagers. *Ingenieur-Archiv* **1963**, *33*, 85–108. [CrossRef]
8. van Buuren, S. *Modeling and Simulation of Porous Journal Bearings in Multibody Systems*; KIT Scientific Publishing: Karlsruhe, Germany, 2014; Volume 21.
9. Chatzisavvas, I. Efficient Thermohydrodynamic Radial and Thrust Bearing Modeling for Transient Rotor Simulations. Ph.D. Thesis, Technische Universität Darmstadt, Darmstadt, Germany, 2018.
10. PW1100G-JM: Geared Turbofan Engine. Available online: https://www.mtu.de/engines/commercial-aircraft-engines/narrowbody-and-regional-jets/gtf-engine-family/ (accessed on 13 May 2024).
11. Dowson, D.; Taylor, C. Cavitation in bearings. *Annu. Rev. Fluid Mech.* **1979**, *11*, 35–65. [CrossRef]
12. Kumar, A.; Booker, J. A Finite Element Cavitation Algorithm: Application/Validation. *J. Tribol.* **1991**, *113*, 255–260. [CrossRef]
13. Dowson, D. A generalized Reynolds equation for fluid-film lubrication. *Int. J. Mech. Sci.* **1962**, *4*, 159–170. [CrossRef]
14. Pinkus, O.; Sternlicht, B.; Saibel, E. Theory of hydrodynamic lubrication. *J. Appl. Mech.* **1962**, *29*, 221–222. [CrossRef]
15. Hamzehlouia, S.; Behdinan, K. Thermohydrodynamic Modeling of Squeeze Film Dampers in High-Speed Turbomachinery. *SAE Int. J. Fuels Lubr.* **2018**, *11*, 129–146. [CrossRef]
16. San Andrés, L.; Vance, J.M. Effects of Fluid Inertia and Turbulence on the Force Coefficients for Squeeze Film Dampers. *J. Eng. Gas Turbines Power* **1986**, *108*, 332–339. [CrossRef]
17. San Andrés, L.; Vance, J.M. Effects of Fluid Inertia on Finite-Length Squeeze-Film Dampers. *ASLE Trans.* **1987**, *30*, 384–393. [CrossRef]
18. Hamzehlouia, S. Squeeze Film Dampers in High-Speed Turbomachinery: Fluid Inertia Effects, Rotordynamics, and Thermohydrodynamics. Ph.D. Thesis, Mechanical and Industrial Engineering, University of Toronto, Toronto, ON, Canada, 2017.
19. Hamzehlouia, S.; Behdinan, K. A study of lubricant inertia effects for squeeze film dampers incorporated into high-speed turbomachinery. *Lubricants* **2017**, *5*, 43. [CrossRef]
20. San Andrés, L. Force coefficients for a large clearance open ends squeeze film damper with a central feed groove: Experiments and predictions. *Tribol. Int.* **2014**, *71*, 17–25. [CrossRef]
21. San Andrés, L.; Jeung, S.H.; Den, S.; Savela, G. Squeeze Film Dampers: An Experimental Appraisal of Their Dynamic Performance. In Proceedings of the First Asia Turbomachinery and Pump Symposium, Singapore, 22–25 February 2016.
22. San Andrés, L.; Koo, B.; Jeung, S.H. Experimental Force Coefficients for Two Sealed Ends Squeeze Film Dampers (Piston Rings and O-Rings): An Assessment of Their Similarities and Differences. *J. Eng. Gas Turbines Power* **2018**, *141*, 021024. [CrossRef]
23. Chatzisavvas, I.; Arsenyev, I.; Grahnert, R. Design and optimization of squirrel cage geometries in aircraft engines toward robust whole engine dynamics. *Appl. Comput. Mech.* **2023**, *17*, 93–104. [CrossRef]
24. Lang, O.R.; Steinhilper, W. *Gleitlager: Berechnung und Konstruktion von Gleitlagern Mit Konstanter und Zeitlich Veränderlicher Belastung*; Springer: Berlin/Heidelberg, Germany, 1978.
25. Rienäcker, A. Instationäre Elastohydrodynamik von Gleitlagern Mit Rauhen Oberflächen und Inverse Bestimmung der Warmkonturen. Ph.D. Thesis, RWTH Aachen, Aachen, Germany, 1995.
26. San Andrés, L.; Delgado, A. A Novel Bulk-Flow Model for Improved Predictions of Force Coefficients in Grooved Oil Seals Operating Eccentrically. *J. Eng. Gas Turbines Power* **2012**, *134*, 052509. [CrossRef]
27. Schmidt, M.; Reinke, P.; Rabanizada, A.; Umbach, S.; Rienäcker, A.; Branciforti, D.; Philipp, U.; Preuß, A.C.; Pryymak, K.; Matz, G. Numerical Study of the Three-Dimensional Oil Flow Inside a Wrist Pin Journal. *Tribol. Trans.* **2020**, *63*, 415–424. [CrossRef]
28. Reinke, P.; Schmidt, M. *Lokale, Hochauflösende 3D-CFD-Simulation der Schmierspaltströmung in Einem Instationär Belasteten Radialgleitlager*; Final Report, No. 1154, FVV e.V.; FVV: Frankfurt/M, Germany, 2014; Volume 1073.
29. Kistner, B. Modellierung und Numerische Simulation der Nachlaufstruktur von Turbomaschinen am Beispiel einer Axialturbinenstufe. Ph.D. Thesis, Technische Universität Darmstadt, Darmstadt, Germany, 1999.
30. Khonsari, M.M.; Booser, E.R. *Applied Tribology: Bearing Design and Lubrication*; John Wiley & Sons, Ltd.: Hoboken, NJ, USA, 2017.

31. Jaitner, D. Effiziente Finite-Elemente-Lösung der Energiegleichung zur Thermischen Berechnung Tribologischer Kontakte. Ph.D. Thesis, University of Kassel, Kassel, Germany, 2017.
32. Hughes, T.J.; Tezduyar, T. Finite element methods for first-order hyperbolic systems with particular emphasis on the compressible Euler equations. *Comput. Methods Appl. Mech. Eng.* **1984**, *45*, 217–284. [CrossRef]
33. Brooks, A.N. A Petrov-Galerkin Finite Element Formulation for Convection Dominated Flows. Ph.D. Thesis, California Institute of Technology, Pasadena, CA, USA, 1981.
34. Codina, R. A discontinuity-capturing crosswind-dissipation for the finite element solution of the convection-diffusion equation. *Comput. Methods Appl. Mech. Eng.* **1993**, *110*, 325–342. [CrossRef]